The Radio-Optical Jet in NGC 3862 from Parsec to Sub-Kiloparsec Scales

L. Lara¹, L. Feretti², G. Giovannini^{2,3}, S. Baum⁴, W.D. Cotton⁵, C.P. O'Dea⁴ and T. Venturi²

ABSTRACT

We have observed the radio source in NGC 3862 (3C264) simultaneously with the EVN and the MERLIN arrays, obtaining detailed images of its radio structure from parsec to sub-kiloparsec scales. 3C264 shows a one-sided jet, with evident variations in its morphological properties with distance. We have analyzed HST optical data of NGC 3862, finding a one-to-one correspondence between radio and optical features in the jet. The radio to optical spectral index is approximately constant along the jet. Synchrotron appears as the most plausible mechanism for the observed jet emission at radio and optical wavelengths. Local particle reacceleration or, alternatively, deviation from the condition of equipartition are plausible mechanisms to explain the low synchrotron cooling and constant spectral index in the jet of 3C264.

Subject headings: galaxies: individual (NGC 3862) – galaxies: jets – radiation mechanisms: nonthermal

¹Instituto de Astrofísica de Andalucía, CSIC, Apdo. 3004, 18080 Granada, Spain

²Istituto di Radioastronomia, CNR, Via Gobetti 101, I-40129 Bologna, Italy

³Dipartimento di Fisica, Universitá di Bologna, via B. Pichat 6/2, I-40127 Bologna, Italy

⁴Space Telescope Science Institute, Baltimore, MD, USA

National Radio Astronomy Observatory, 520 Edgemont Road, Charlottesville, VA 22903-2475, USA

1. Introduction

The interstellar medium plays a crucial role in the spatial evolution of extragalactic radio jets. There is increasing evidence that interaction with the surrounding environment causes jets in Fanaroff-Riley type I radio sources (FR I; Fanaroff & Riley 1974) to decelerate from initially relativistic to sub-relativistic bulk velocities, and that such interaction determines the morphology of their large scale structures (Parma et al. 1996). Observations of FR I radio sources at parsec scales made with very long baseline interferometry (VLBI) show, in most cases, one-sided core-jet morphologies. This fact is thought to be a strong indication of the existence of relativistic flows in the inner parts of FR I jets (Giovannini et al. 1994; Lara et al. 1997). On the other hand, observations on the kiloparsec scale show structures consisting of a core and two jets with brightness ratio close to unity, thus indicating that relativistic boosting of the radio emission is negligible at larger distances from the core (Parma et al. 1996). Current models for FR I radio sources postulate that deceleration of the plasma flow from relativistic to subrelativistic speeds occurs within 10 - 3000 pc from the active core (Bicknell 1994; Laing 1994). Needless to say the importance of studying in detail the regions where the velocity transition is supposed to take place in FR I jets in order to understand the mechanisms of plasma deceleration. However, detailed radio images of the sub-kiloparsec regions of jets in FR I radio sources are not common in the literature, mainly due to the lack of sensitive interferometric arrays at these scales. This difficulty can be overcome via the combination of different arrays. Moreover, the few known sources where jets are observed at wavelengths other than radio are extremely interesting, since broadband studies can largely constrain the proposed physical models.

In this framework, we present and discuss here the results derived from simultaneous observations with the European VLBI Network (EVN) and the Multi Element Radio Linked Interferometer Network (MERLIN) of the FR I radio source 3C264 (B 1142+198) at 5 GHz. The combination of both instruments provides the angular resolution suitable to map with great detail the radio structure of 3C264 from parsec to sub-kiloparsec scales. The large scale structure of 3C264 is well known: it exhibits a head-tailed morphology with a prominent core and a wiggling jet extending towards the northeast, which ends in a blob

of emission at 35" from the core (Gavazzi et al. 1981; Bridle & Vallée 1981; Baum et al. 1988). There is some evidence of emission from the counter-jet at about 11" southwest from the core (Lara et al. 1997). Both the jet and possible counter-jet are embedded in a vast and diffuse emission which seems to be dragged along the north, revealing the existence of a dense intergalactic medium. In fact, 3C264 is optically identified with NGC 3862 ($m_v = 13.67$; z = 0.0216), a bright galaxy in the cluster Abell 1367. It contains a compact (\sim 2") and possibly variable X-ray source embedded in the diffuse X-ray emission from the hot halo of the cluster, in a position consistent with that of the central 5 GHz radio source component (Elvis et al. 1981; Prieto 1996).

NGC 3862 is peculiar because it harbors an optical jet in a position angle coincident with that of the radio jet (Crane et al. 1993; Baum et al. 1997). The optical jet, observed with the HST, extends up to 2". There is also evidence of a "ring" around the core, with a radius between 0.75" and 1" (Baum et al. 1997, hereafter BOG97). The region inside this ring seems to be cleared out of dust by the jet or, most probably, by some other nuclear related process (Hutchings et al. 1998). Line-emitting gas is also found in the core region, although it is not spatially correlated with the jet emission (BOG97).

We assume a Hubble constant $H_0 = 75 \text{ km s}^{-1}$ Mpc⁻¹ and a deceleration parameter $q_0 = 0.5$, and define the spectral index, α , such that $S_{\nu} \propto \nu^{-\alpha}$. In 3C264, 1 mas corresponds to 0.4 pc in linear distance.

2. Observations and Data Analysis

We observed 3C264 simultaneously with the EVN and MERLIN on 1995 May 22. The observations were made at the frequency of 5 GHz in left circular polarization (LCP) at the VLBI antennas, and dual polarization at the MERLIN antennas. The bright radio sources 4C39.25 and 1144+402 were also observed as fringe finders for the correlation of the VLBI data, and as point source calibrators.

The MERLIN array consisted of six antennas (Tabley, Cambridge, Jodrell-MK2, Darnhall, Knockin and Defford, all located in England), with minimum and maximum baselines of 130 k λ and 2.2 M λ , respectively, recording a bandwidth of 15 MHz. Flux density calibration of the MERLIN data was performed with the OLAF package by comparison of OQ208 and 1144+402 with the primary flux density calibra-

tor 3C286 (see BOG97 for a complete description of MERLIN observations and data reduction).

The EVN array consisted of seven antennas: Effelsberg (Germany), Cambridge and Jodrell-MK2 (U.K.), Medicina and Noto (Italy), Onsala (Sweden) and Westerbork (The Netherlands). The minimum and maximum baseline separation were 3.7 and 38 M λ , respectively. The EVN stations used the Mark-III recording system (Rogers et al. 1983) with a synthesized bandwidth of 28 MHz (mode B). The VLBI data from the different telescopes were correlated in absentee at the Max-Planck-Institut für Radioastronomie in Bonn (Germany). Cambridge did not yield VLBI fringes due to technical problems during the recording of the data. The calibration of the visibility amplitudes was performed with the NRAO Astronomical Image Processing System (AIPS). In addition, the correction of the fringe rate through the so-called global fringe fitting (Schwab & Cotton 1983) was applied.

We used the Caltech Difmap package (Shepherd et al. 1994) and the AIPS package for imaging the EVN and the MERLIN data, respectively, following standard self-calibration and mapping procedures. Once the separate maps from each array were produced, we proceeded to combine the self-calibrated EVN and MERLIN data. The different calibration schemes applied to each data set resulted in a slight misalignment between the MERLIN and EVN flux density scales. Considering that MERLIN is sensitive to extended emission which is resolved out by the EVN, and that the flux density calibration of MERLIN was made using a primary flux density calibrator, we adjusted the EVN flux density scale to fit the more reliable MERLIN scale.

Final maps from the combined data set were obtained with the Difmap package. The EVN image, which reproduces well the data from longer baselines, was taken as the initial source model in the mapping procedure. In order to find a suitable delta-component model able to reproduce the visibility data at all uv-spacings, we allowed CLEAN to act progressively on more and more further regions along the jet. Data with large uv-spacings were also weighted less by applying progressively stronger Gaussian uv-tapers in order to gain sensitivity to more extended emission after each self-calibration and CLEAN iteration.

3. Results

3.1. The Jet from Parsec to Sub-kiloparsec Scales

In Fig.1 we present images of the radio jet in NGC 3862, ordered from highest (6.0 mas \times 3.6 mas), at top-left, to lowest (62 mas \times 52 mas) angular resolution, at top-right. Details of the radio structure from scales of several parsecs to scales of \sim 0.5 kpc are evident.

The EVN map in Fig.1a shows an unresolved core and a smooth one-sided jet extending up to 25 mas from the core along position angle (P.A.) $\sim 27^{\circ}$. From Fig.1a it is difficult to identify discrete components in the innermost jet of 3C264. The comparison of this map with a previous global VLBI map made at the same frequency (Lara et al. 1997) shows that, at the level of resolution provided by the EVN, there is no indication of variability of the structure on a time scale of two years, while flux density variability might exist within a 10% level.

Fig.1a shows hints of emission at a distance of 55 mas (22 pc) northeast from the core. A well defined component is evident at this position when MERLIN data are used (Fig.1b). From this component on, the jet appears narrow, well collimated and slightly curved towards the east. In fact, the jet position angle changes from 27° in the inner jet regions, to 44° at ~ 250 mas from the core. This collimated region is distinguished by several knots and by a slowly decaying surface brightness (Fig.1c). At 250 mas (100 pc) from the core there are important changes in the jet characteristics: the opening angle of the jet increases abruptly, and the flow becomes apparently more turbulent. We observe filamentary emission, pronounced kinks and wiggles which suggest the existence of oscillations in the ridge line of the jet, or alternatively, a three dimensional helical structure evolving along three great loops (Fig.1c-d-e). The cone angle of the observed oscillations is about 15°. This possible oscillating or helical structure is also marginally visible in the region between 50 and 100 pc from the core.

The lower resolution maps (Fig.1e-f) show a sharp cut in the jet surface brightness at a distance of 0.8 asec from the core (~ 320 pc), and a deflection of the ridge line. This deflection could be related with an abrupt change in the external medium, perhaps associated with the transition of the jet from the central region, cleared out of dust, to the region outside

the ring (BOG97; Hutchings et al. 1998). With the sensitivity of the observing array, the jet emission is detected up to a distance of 1.2 asec.

The MERLIN array, without Cambridge, recorded both left and right hand circular polarizations. We made a map of the polarized emission of 3C264, although with lower angular resolution (156 mas ×100 mas, P.A. -53°) if compared with the total intensity maps, due to the lack of the longer MERLIN baselines. Although some problems with the calibration could not be definitely solved (the rms noise level of the final image was 0.12 mJy/beam), significant polarization is detected in a small region (2 beam area) at a distance of 170 pc from the core. In this region the projected magnetic field appears parallel to the jet axis and the average degree of polarization is 16%.

There is no evidence of a counter-jet in any of the maps in Fig.1. Lower limits of the jet to counter-jet brightness ratio (R) of 3C264 obtained with different angular resolutions at different positions along the jet are presented in Table 1. To compute R, we assume that the emission from the counter-jet is lower than or equal to 3 times the rms noise level of the image, measured over large empty regions of the maps.

In summary, four distinct parts can be distinguished in the jet of 3C264, indicating that it does not expand at a constant rate as would a steady free jet: i) the strong compact core and smooth innermost jet region (0 - 10 pc); ii) a narrow and well collimated region which extends up to 110 pc; iii) a region where the jet widens, showing kinks and filaments which suggest an oscillating or a helical jet. This region has a projected magnetic field predominantly parallel to the jet axis (100 - 300 pc); iv) a faint and narrow region appearing after a strong jet deflection, possibly due to interaction with the ring (300 - 430 pc).

3.2. Comparison of Radio and Optical Emission

As already noted in BOG97, the optical and radio emission from the jet in NGC 3862 show a remarkably similar structure. A detailed comparison of HST and radio images faces up to the problem of how reliable is the subtraction of the surface brightness from the elliptical host galaxy in order to highlight the optical jet. Fig.4 in BOG97 shows the optical jet of NGC 3862, with deep negative contours surrounding the core. Brightness profiles taken at several position

angles around the core suggest that the subtracted elliptical galaxy model overestimates the optical emission in the inner ~ 70 pc, thus producing the observed negative contours. This region will not be considered in this Section. We also note that a factor of 2 must be applied to the flux density scale in the optical image of NGC 3862 in BOG97, because a change in the software used to combine the images for cosmic ray removal caused confusion over whether the image header was updated with the sum of the exposure times.

To compare the radio and the HST images, both were convolved with a circular Gaussian beam of 45 mas. The images were then registered by the peak of brightness of the core in the two maps. Opacity effects on the position of the core are assumed to be negligible compared with the actual resolution of 45 mas. We find that, beyond a distance of 100 pc from the core, there is good correspondence of radio and optical features in the map. Fig.2a shows brightness profiles of the radio and optical flux density along the ridge line of the jet. The optical emission has been multiplied by a constant factor for display purposes. There are five distinct peaks at radio wavelengths and four peaks at optical wavelengths. Peak positions in the optical correspond to peak positions in the radio, except for the first knot at ~ 90 pc from the core, which seems to be shifted outwards at optical wavelengths. We however note that this shift could be a consequence of the elliptical image subtraction in the inner regions of NGC 3862.

The radio-to-optical spectral index along the jet, obtained with a resolution of 45 mas, is displayed in Fig.2b. It shows slight variations around a mean value of 0.63, very similar to that found by Biretta et al. (1991) in the jet of M87. We estimate errors of the order of 0.02 (corresponding to 1 σ , including the rms noise level of each image plus a 15% error in the flux density scale). The knots show a steeper spectrum than the inter-knot regions, with differences in the spectral index of about 0.05, thus marginally significant if compared with the measurement uncertainties. However, Hutchings et al. (1998) report from HST optical spectroscopy that the knots are brighter at shorter wavelengths. The steeper spectrum we find in the knots results from the less contrast observed between jet-knot brightness in the optical than in the radio (Fig.2a), a feature which might be real but also consequence of the subtraction of the background galaxy emission.

We have measured the flux density of the jet in NGC 3862 using present radio observations at 5 GHz, recent 1.6 GHz MERLIN observations (to be published elsewhere), optical data in BOG97, data available in the HST public archive, and data from the literature (Table 2). Flux density of the radio jet has been estimated in AIPS measuring first the total flux density over the region where optical emission is observed, including the core, to which the integrated flux density of a Gaussian component which fits the core emission is later subtracted. The HST optical data have been analyzed using IRAF: we removed the cosmic-ray hits with the task CRREJ, and constructed a set of four images by rotating the original one 0° , 90° , 180° and 270° , with the core peak of brightness at the rotation center. The median of these four images, a good approximation to the galaxy core and background emission, was subtracted from the original image to isolate the jet.

The broadband spectrum of the jet is displayed in Fig.3. The radio spectral index (α_r) is 0.46, and the optical spectral index (α_{opt}) is 1.34. Crane et al. (1993) report a similar optical spectral index for the jet $(\alpha_{opt}=1.4)$ from HST observations at two wavelengths, although their flux density values are much higher (a factor of 2.5) than the values derived by us. Flux density variability seems an unlikely reason for this large discrepancy, since only a very low level of variability is observed at radio wavelengths. For the sake of consistency, Crane et al. (1993) data have not been used in the previous estimation of the optical spectral index, and will not be used for further discussion.

The Rosat X-ray flux density (Prieto 1996) is also plotted in Fig.3. This measurement is clearly an upper limit due to the low angular resolution (25") of the X-ray observations. In fact, Prieto finds that no single power law can be fit to the compact X-ray emission, indicating that it might be contaminated by the contribution from a thermal component.

4. Discussion

4.1. Jet Dynamics

¿From Fig.1 it is evident that the jet of 3C264 does not expand at a constant rate. It appears narrow and well collimated during the first 100 pc, and widens further on, apparently becoming turbulent. Deceleration between parsec and kiloparsec scales in 3C264 was suggested by Lara et al. (1997) from jet

to counter-jet brightness ratio arguments, assuming an intrinsic symmetric structure. Moreover, BOG97 deduced an important jet deceleration between 300 and 400 pc from the core, modeling the emissivity of an adiabatic expanding jet. Deceleration was then explained through a change of properties in the external medium associated with the existence of the circumnuclear ring, and an initial velocity of 0.98c was required in order to make compatible the observed jet to counterjet brightness ratio with the adiabatic model predictions.

The very high resolution of the present radio observations allows us to study the jet dynamics from a few parsecs up to 300 pc from the core. From similar arguments to those discussed in BOG97, i.e. assuming adiabatic expansion and a magnetic field oriented predominantly parallel to the jet axis, we obtain that in order to compensate for the dramatic expansion of the jet opening angle at 100 pc and keep the predicted surface brightness comparable to that observed, the jet has to decelerate in the region between 100 and 200 pc from 0.98c to 0.85c. However, this result faces two main difficulties: first, the observed degree of polarization implies an important contribution of random field in 3C264, so that assuming a parallel and uniform magnetic field may be not a good assumption. Second, if the jet had an oscillating or helical structure, our estimate of the evolution of the jet width would be misleading, seriously affecting the prediction of the adiabatic expanding model. In conclusion, although deceleration between parsec and kiloparsec scales is rather plausible in 3C264 (Lara et al. 1997), the lack of an observed counter-jet at sub-kiloparsec scales and the difficulties inherent to the adiabatic model do not allow us to precisely determine if deceleration is taking place at these scales. The dramatic widening of the jet at 100 pc from the core could also be due to the jet entering a region of decreased external pressure, rather than to deceleration of the jet.

4.2. Estimation of Physical Parameters

We obtained surface brightness profiles perpendicular to the jet main axis at several positions along the jet, and then measured the jet FWHM and the surface brightness at the ridge line from Gaussian fits. The deconvolution of jet width and surface brightness was done following Appendix A in Killeen et al. (1986). We used the standard formulae of synchrotron radiation (e.g. Miley 1980) to calculate the minimum energy density (u_{me}) at these positions and

the corresponding effective magnetic field B_{me} , which is approximately the equipartition field. The total pressure is assumed to be that of equipartition between particles and magnetic field, $P_{eq} = 0.62 u_{me}$. The effects of Doppler boosting were taken into account assuming a constant jet velocity of 0.98c up to 300 pc from the core (BOG97). In addition, the following assumptions were made in the calculations: i) the magnetic field is assumed to be random; ii) the energy of particles is equally stored in the form of relativistic electrons and heavy particles; iii) lower and upper frequency cutoffs were set to 10 MHz and 10⁵ GHz, respectively; iv) the spectral index of the jet is 0.5 (Fig. 3); and v) the line-of-sight depth is equal to the deconvolved FWHM of the jet corrected for projection effects. We assume that the jet axis forms an angle of 50° with respect to the observer's line of sight (such jet orientation was taken from BOG97 and is in agreement with the constraints in Lara et al. (1997) derived from jet to counter-jet brightness ratio and core prominence). An upper frequency cutoff of 10⁵ GHz was assumed in order to allow synchrotron emission at optical wavelengths (see also Section 4.3.2). However, for the given spectral index, the results on the minimum energy, pressure and magnetic field are not very sensitive to this parameter. The results obtained at different positions along the jet are listed in Table 3 and displayed in Fig.4, as a function of the filling factor η .

The dependences of the magnetic field on the jet width (Φ) and on the distance from the nucleus (D)could be fit with similar power laws of the form $B_{me} \propto \Phi^{-0.8}$ (Fig.4c) and $B_{me} \propto D^{-0.8}$ (Fig.4d). In an adiabatic expanding jet, the expected trends of the magnetic field with the jet width are $B_{\perp} \propto \Phi^{-1}$ and $B_{\parallel} \propto \Phi^{-2}$ (BOG97 and references therein). Identical expected trends are derived for the magnetic field with the distance from the core (Hughes et al. 1989). We obtain dependences closer to Φ^{-1} and D^{-1} , appropriate for a jet with an uniform magnetic field perpendicular to the jet direction. However, only in a small region of 3C264 we observe a projected magnetic field parallel to the jet main axis with a degree of polarization of 16%, which implies that the ordered magnetic field is 47% of total in this region, being the rest oriented randomly (if Faraday depolarization is ignored at 5 GHz). If the jet of 3C264 were purely adiabatic, we would expect trends of the magnetic field with slopes between -1 and -2 (see Section 4.3.2) for further discussion).

4.3. Mechanisms for Optical Emission in Jets

There is an increasing number of radio jets for which optical counterparts have been observed: 3C273. M87, PKS 0521-36, 3C66B, 3C264 (see Sparks et al. 1994 for a review), 3C78 (Sparks et al. 1995), 3C200, 3C346 (de Koff et al. 1996), 3C212, 3C245 (Ridgway & Stockton 1997), 3C371 (Nilsson et al. 1997), and 3C15 (Martel et al. 1998). The understanding of optical emission spatially coincident with synchrotron radio emission in jets is an open question. In principle, if the radiation mechanism at optical wavelengths were synchrotron, we would not expect to detect optical emission at large distances from the core since radiation losses of electrons emitting at visible wavelengths are orders of magnitude larger than those of electrons emitting at radio wavelengths (Felten 1968). However, this is not the case, and optical jets of kiloparsec lengths exist. Several scenarios have been proposed to solve this discrepancy, mostly based on observations of the well studied M87 radio source: i) First-order Fermi reacceleration of electrons in the knots of a jet. ii) The existence of a high field boundary layer surrounding a low magnetic field channel through which the relativistic electrons are conducted, with negligible synchrotron losses, to the place where they cross the high field shell and radiate (Owen et al. 1989). iii) Local reacceleration processes occurring all along the jet, which maintain roughly constant the maximum cutoff energy of the electron population. Spectral and brightness variations are produced by changes in the magnetic field strength, which dominates the appearance of the jet (Meisenheimer et al. 1996). iv) Magnetic field below equipartition and adiabatic fluctuations, combined with Doppler beaming effects (Heinz & Begelman 1997).

Of course, different explanations for optical emission aligned with radio jets are possible if different emission mechanisms are invoked. Besides synchrotron, radiation at optical wavelengths could be produced i) by inverse Compton scattering of photons by relativistic electrons in the jet, ii) by Thomson scattering of anisotropic light emitted from the core, iii) by thermal bremsstrahlung emission from clumped hot gas, or iv) in jet-induced star-formation regions (see Daly 1992 for a detailed discussion). In NGC 3862, the radio and the optical emission are spatially coincident, with peaks in the radio corresponding to peaks in the optical, except the first knot which, as noted in Section 3.2, could be affected by the galaxy subtraction. This implies that the radia-

tion from both parts of the spectrum answer in the same way to the local variations in the physical conditions. This fact renders rather unplausible for the optical radiation any mechanism which is not directly related to the synchrotron radiation observed at radio wavelengths. In addition, the thrust of the relativistic flow might have swept any thermal gas in the region occupied by the jet itself, leaving Thomson or bremsstrahlung processes constrained to regions well outside the jet axis, and thus not spatially coincident with the synchrotron radiation. Note also that Hutchings et al. (1998) find no optical emission lines associated with the jet.

In the next sections we will concentrate on two possible mechanisms for the optical radiation which are directly related with the synchrotron processes responsible for the radio emission: inverse Compton scattering (IC) and synchrotron itself.

4.3.1. Inverse Compton Scattering

Following Blumenthal & Tucker (1974) we have derived the temperature of an external radiation field described by a Planck distribution which is IC scattered by the population of relativistic electrons in the jet:

$$T = \left[\frac{4.05 \times 10^{18}}{4884^{\alpha}} \cdot \frac{a}{b} \cdot B^{1+\alpha} \left(\frac{\nu_{opt}}{\nu_{rad}} \right)^{\alpha} \frac{S_{ic}}{S_s} \right]^{\frac{1}{3+\alpha}}, (1)$$

where $\alpha (= 0.5)$ is the spectral index, assumed constant along the jet; a and b are two spectral index dependent functions ($\frac{a}{b} = 0.02$ for $\alpha = 0.5$); B is the average effective magnetic field, which we have obtained from minimum energy assumptions ($B \sim 0.7$ mG in the region where strong optical radiation is observed); $\nu_{opt}(=4.35\times10^{14} \text{ Hz})$ and $\nu_{rad}(=5\times10^9 \text{ m})$ Hz) are the observing frequencies of optical and radio emission, respectively; S_{ic} and S_s are the jet flux densities measured at optical and radio wavelengths, respectively (see Table 2). From equation 1 we obtain a black body temperature of 590 K, which, according to Wien displacement law, corresponds to the maximum energy emitted at a frequency of 3.5×10^{13} Hz $(9\mu m)$. A hot dusty region could be responsible of such radiation field in the infrared. The integrated flux density derived at $60\mu m$ from a region with a radius of 400 pc turns to be of the order of 10^4 Jy, which is indeed much higher than the observed 220 mJv at this wavelength (Hes et al. 1995). Thus, we conclude that it is unlikely that the optical jet emission is produced by IC scattering of an external radiation field.

In a similar way, we can estimate the ratio of the IC and synchrotron radiation, assuming this time that the synchrotron photons from the jet are IC scattered by the relativistic electrons (see Hughes & Miller 1991):

$$\frac{I_{\nu,ic}}{I_{\nu,s}} = \frac{16\pi g \mathcal{F}(\alpha)}{\sqrt{3} \left(\frac{3}{2\pi}\right)^{\alpha} c_{5}^{(\alpha)}(\alpha)} \cdot \frac{4\pi \epsilon_{o} c \sigma_{T}}{e^{2}} \cdot I_{\nu,s} \ \nu_{s}^{2\alpha} \ \ln\left(\frac{\nu_{u}}{\nu_{l}}\right)$$
$$\left(\frac{3\nu_{ic}}{4}\right)^{-\alpha} \cdot \left(\frac{eB}{m_{e}}\right)^{-(\alpha+1)} \cdot \left(\frac{\mathcal{D}}{1+z}\right)^{-(\alpha+3)}.$$

In this formula, expressed in SI units, g is a geometrical factor to allow for possible anisotropy of the photon and electron distributions; \mathcal{F} and $c_5^{(\alpha)}$ are spectral index dependent functions (see reference for exact definition). In our case, $\alpha=0.5$, $\mathcal{F}(\alpha)=0.455$ and $c_5^{(\alpha)}(\alpha)=2.945$; σ_T is the Thomson cross-section; ϵ_o is the permittivity of free space; c is the velocity of light; e is the charge of an electron; ν_s , ν_{ic} , ν_u and ν_l are the frequency of synchrotron radiation (5 GHz), IC scattered radiation (4.35 × 10⁵ GHz), and upper (100 GHz) and lower (0.01 GHz) limits to frequency spectrum, respectively; B is the magnetic field $(7 \times 10^{-8} \text{ T})$; m_e is the electron mass; \mathcal{D} is the Doppler factor.

We obtain that

$$\frac{I_{\nu,ic}}{I_{\nu,s}} \simeq 2.2 \times 10^{-9} \ g \ \mathcal{D}^{-3.5},$$
 (2)

which has to be compared with an observed ratio of 8×10^{-4} . If we assume $g \simeq \mathcal{D} \simeq 1$, then the predicted optical emission is several orders of magnitude too low making it unlikely that the IC mechanism is responsible for the optical emission. IC emission would be consistent with the data only for $\mathcal{D}=0.03$ if $g\simeq 1$. Such a low Doppler factor would require the jet (and counter-jet) bulk velocity to be very close to c ($\beta \geq 0.9995$), which is a very high velocity if compared with other well studied radio jets, but in addition, would render 3C264 one of the intrinsically brightest sources on the sky, which contrast with the level of emission from the lobes and with its classification as an FR I radio source.

In summary, we conclude that IC is not a plausible mechanism for the jet optical emission in NGC 3862.

4.3.2. Synchrotron Emission

Previous arguments and the broadband spectrum in Fig.3 suggest synchrotron as the most plausible

mechanism of emission from radio to optical wavelengths in the jet of NGC 3862. In consequence, we have fit three different synchrotron spectral aging models to the broadband spectrum of the jet: the continuous injection (CI) model, the Kardashev-Pacholczyk (KP) model, and the Jaffe-Perola (JP) model (Kardashev 1962; Pacholczyk 1970; Jaffe & Perola 1973). These models assume an initial powerlaw distribution of particles. The CI model considers a continuous injection of fresh particles in the distribution, while the KP and JP models assume a single "one-shot" injection of particles. The JP model allows for isotropization of particles pitch-angle, while the KP model assumes constant pitch-angles. Each model is characterized by an injection spectral index and a break-frequency above which the spectrum steepens. We obtain that an injection spectral index of 0.5 is valid for all three models, with break frequencies equal to 4.3×10^{13} Hz, 2.2×10^{14} Hz, and 4.3×10^{14} Hz for the CI, KP and JP models, respectively (Fig.5). The KP model provides a slightly better fit (χ^2) than the CI or JP models, although our data are not adequate to discern any significant differences in these models.

Optical synchrotron radiation requires high energy electrons, with γ of the order of 10^6 , which imply short synchrotron cooling times. With the magnetic field derived from minimum energy assumptions (B_{me} (Gauss)), and the upper frequency cutoff derived from the KP model (ν_b (GHz)), we estimated the mean synchrotron lifetime at several positions along the jet, $\langle t_s \rangle$ (Miley 1980):

$$< t_s > (yr) = 0.82 B_{me}^{\frac{1}{2}} \left(B_{me}^2 + B_{MW}^2 \right)^{-1} (1+z)^{\frac{-1}{2}} \nu_b^{\frac{-1}{2}}$$
(3)

where $B_{MW} = 3.5 \times 10^{-6} (1+z)^2$ (Gauss) is the equivalent magnetic field of the microwave background. The result is that the lifetime increases smoothly with the distance from the core (see Table 3), reaching a maximum value of only 190 yr at 300 pc.

Assuming a lifetime of the order of 2×10^2 yr, the electrons must have been accelerated, at the most, at a distance of 60 pc (150 mas) from the location where radiation is being produced. Reacceleration by Fermi processes in shocks would then require the existence of well defined knots all along the jet of 3C264, which we do not observe in our maps. In addition, it is known that Fermi reacceleration finds difficulties in explaining the constancy of radio to optical spectral index in M87 (Heinz & Begelman 1997). Similar

difficulties would arise for 3C264, which also shows a rather uniform radio to optical spectral index. The slight steepening of the spectrum in the brightness peaks (Fig.2), if real, would indicate that these are regions of more efficient energy dissipation at higher frequencies, rather than places of particle reacceleration, and could hardly be associated with the shocks required by the Fermi mechanism.

If the wiggles observed in 3C264 were signs of a helical structure wrapped around an empty cone, then it would be possible to invoke the hollow channel model (Owen et al. 1989) to explain the lack of synchrotron cooling and the observed optical emission. We note however, that this scenario has some difficulties associated with the prediction of instabilities produced by the drift of electrons from the low field channel to the high field boundary layer, which would quickly isotropize the beam (Achatz et al. 1990; Meisenheimer et al. 1996). Our observations do not currently rule out the hollow channel model. We note that a CI spectrum would be more suitable to describe such scenario. Observations over broader frequency range are needed to test it.

The constant radio-to-optical spectral index in the jet of 3C264 could be explained with the local reacceleration model (Meisenheimer et al. 1996) or, alternatively, with the model by Heinz & Begelman (1997). In both cases, the appearance of the jet is dominated by the fluctuations of the magnetic field. The derived dependence of the magnetic field with the distance from the core of 3C264 ($B \propto D^{-0.8}$) is smooth, if compared with the expected trend of an adiabatic expanding jet $(B \propto D^{[-1,-2]})$. A similar behavior is also found in the jet of M87 (Meisenheimer et al. 1996). Such smooth dependence is consistent with the existence of mechanisms of field regeneration or amplification in the jet (Hughes et al. 1989). For example, regeneration of the magnetic field could be produced by turbulence in the jet flow, which in addition is also an efficient mechanism of local particle reacceleration (Eilek & Hughes 1991). Another possible explanation for the slow evolution of the magnetic field in 3C264 is that the expansion of the jet could be highly influenced by the properties of the external medium, instead of being adiabatic. In fact, the morphology of the radio jet clearly indicates that it is not expanding freely, and that the influence of the external medium might be important. Finally, as suggested for M87 by Heinz & Begelman (1997), the possibility exists that the condition of equipartition, which is under all previous calculations but without a strong justification, is not valid in 3C264.

In summary, although the mechanism which maintains or provides the energy of the electrons in the jet of 3C264 remains unclear, the constancy of the jet radio to optical spectral index suggests that local reacceleration or departures from equipartition are the most plausible scenarios for the jet optical emission.

5. Conclusions

We have presented and discussed combined EVN + MERLIN data of the radio galaxy 3C264. Detailed images of the radio structure from parsec to sub-kiloparsec scales have been obtained, showing four different regions in the jet: i) the strong compact core and smooth innermost jet (0 - 10 pc): ii) a well collimated and narrow region (10 - 100 pc); iii) a region with strong widening, kinks and filaments, which could be interpreted as a helical or oscillating jet (100 - 300 pc); iv) a faint and narrow region appearing after a strong jet deflection (300 - 430 pc). We have shown that there is good correspondence between optical and radio features in the jet of 3C264. Moreover, the radio to optical spectral index is approximately constant all along the jet.

The application of an adiabatic expansion model to the jet of 3C264 requires deceleration of the plasma flow between 100 and 200 pc in order to compensate for the expansion of the jet in this region and reproduce the observed surface brightness. However, the observed magnetic field configuration and the external medium, which could influence the jet expansion, renders this result dubious.

Possible mechanisms for optical emission in the jet of 3C264 are discussed, with synchrotron being the most plausible. The integrated broadband spectrum can be better fit with a KP synchrotron aging model. We derive an injection spectral index of 0.5 and a break frequency between radio and optical wavelengths of $\sim 2 \times 10^{14}$ Hz. However, more data covering a wide range of frequencies and spatial resolutions are necessary to clearly discriminate between the different models, and to make detailed studies of the spectral evolution along the jet.

We have estimated physical parameters along the jet under minimum energy considerations. The trend of the equipartition magnetic field with distance does not agree with expectations in an adiabatic expanding jet. The discrepancy could be due either to incorrect assumptions (geometry of the magnetic field), or to special physical conditions (deviations from equipartition, existence of amplification of the magnetic field). The existence of local reacceleration or, alternatively, departures from the condition of equipartition are possible scenarios to explain the constant spectral index and the low synchrotron cooling in the jet of 3C264.

The radio structure found in 3C264, that is, a well collimated narrow jet which suddenly widens, is not unique. Similar radio structures are seen in many other FR-I sources. If the condition of similar radio morphology could be generalized to the condition of similar physical properties, then a large number of FR-I jets emitting also optical synchrotron radiation should be expected.

We acknowledge Dr. Antonio Alberdi and Dr. Alan Bridle for their valuable comments on the manuscript, and Matteo Murgia for allowing us to use his code SYNAGE. This research was supported in part by the Spanish DGICYT research grant PB94-1275. LL wishes to acknowledge support for this research by the European Union under contract ERBFMGECT 950012. The National Radio Astronomy Observatory is a facility of the National Science Foundation operated under cooperative agreement by Associated Universities, Inc. This work was based on observations made with the NASA/ESA Hubble Space Telescope, obtained from the data archive at the Space Telescope Science Institute.

REFERENCES

Achatz, U., Lesch, H. and Schlickeiser, R., 1990, A&A, 233, 391

Baum, S. A., Heckman, T., Bridle, A., van Breugel, W. & Miley, G. 1988, ApJS, 68, 643

Baum, S. A., O'Dea, C. P., Giovannini, G., Biretta,
J., Cotton, W. D., de Koff, S., Feretti, L.,
Golombek, D., Lara, L., Macchetto, D., Miley, G.
K., Sparks, W. B., Venturi, T., Komissarov, S. S.,
1997, ApJ, 483, 178

Baum, S. A., O'Dea, C. P., Giovannini, G., Biretta,
J., Cotton, W. D., de Koff, S., Feretti, L.,
Golombek, D., Lara, L., Macchetto, D., Miley, G.
K., Sparks, W. B., Venturi, T., Komissarov, S. S.,
1998, ApJ, 492, 854 (erratum)

- Bicknell, G. V. 1994, ApJ, 422, 542
- Biretta, J.A., Stern, C.P. & Harris, D.E. 1991, AJ, 101, 1632
- Blumenthal, G. R. and Tucker W. H. 1974, X-Ray Astronomy, R. Giacconi & H. Gursky, Dordrecht: Reidel, 1974, 99
- Bridle, A.H., & Vallée, J.P. 1981, AJ, 86, 1165
- Crane, P., Peletier, R., Baxter, D. et al. 1993, ApJ, 402, L37
- Daly, R. 1992, ApJ, 399, 426
- de Koff, S., Baum, S. A., Sparks, W. B., Biretta, J., Golombek, D., Macchetto, F., McCarthy, P. and Miley, G. K. 1996, ApJS, 107, 621
- Eilek, J.A. & Hughes, P.A. 1991, Beams and Jets in Astrophysics, P.A. Hughes, Cambridge University Press, 1991, 428
- Elvis, M., Schreier, E. J., Tonry, J., Davis, M. & Huchra, J. P. 1981, ApJ, 246, 20
- Fanaroff, B. L. & Riley, J. M. 1974, MNRAS, 167, 31
- Felten, J. E. 1968, ApJ, 151, 861
- Gavazzi, G., Perola, C. G. & Jaffe, W. 1981, A&A, 103, 35
- Giovannini, G., Feretti, L., Venturi, T., Lara, L, Marcaide, J.M., Rioja, M.J., Spangler, S.R & Wehrle, A.E. 1994, ApJ, 435, 116
- González-Serrano, J. I., Carballo, R. & Pérez-Fournon, I. 1993, AJ, 105, 1710
- Heinz, S. & Begelman, M.C., 1997, ApJ, 490, 653
- Hes, R., Barthel, P.D. & Hoekstra, H. 1995, A&A, 303, 8
- Hughes, P.A., Aller, H.D. & Aller, M.F. 1989, ApJ, 341, 54
- Hughes, P. A. and Miller, L. 1991, Beams and Jets in Astrophysics, P.A. Hughes, Cambridge University Press, 1991, 1
- Hutchings, J. B., Baum, S. A., Weistrop, D., Nelson, C., Kaiser, M. E., Gelderman, R. F, 1998, ApJ, in press

- Jaffe, W. J. & Perola, G. C., 1973, A&A, 26, 423
- Kardashev, N. S., 1962, Soviet Astron. AJ, 6, 317
- Killeen, N.E.B., Bicknell, G.V., Ekers, R.D., 1986, ApJ, 302, 306
- Laing, R. A. 1994, The Physics of Active Galaxies, G. V. Bicknell, M. A. Dopita & P. J. Quinn, ASP Conference Series, Vol. 54, 227
- Lara, L, Cotton, W.D., Feretti, L., Giovannini, G., Venturi, T., Marcaide, J.M., 1997, ApJ, 474, 179
- Martel, A. R., Sparks, W. B., Macchetto, D., Biretta, J. A., Baum, S. A., Golombek, D., McCarthy, P. J., de Koff, S., and Miley, G. K. 1998, ApJ, 496, 203
- Meisenheimer, K., Röser, H.-J. & Schlötelburg, M., 1996, A&A, 307, 61
- Miley, G. K. 1980, A&A Rev., 18, 165
- Nilsson, K., Heidt, J., Pursimo, T., Sillampaa, A., Takalo, L.O. & Jager, K., 1997, ApJ, 484, 107
- Owen, F. N., Hardee, P.E. & Cornwell, T.J. 1989, ApJ, 340, 698
- Pacholczyk, A. G., 1970, Radio Astrophysics (San Francisco: Freeman)
- Parma, P., De Ruiter, H.R. & Fanti, R. 1996, Extragalactic Radio Sources, R. Eckers, C. Fanti & L. Padrielli, Kluwer Academic Publishers, 1996, 137
- Prieto, M.A. 1996, MNRAS, 282, 421
- Rybicki, G.B. and Lightman, A.P. 1979, Radiative Processes in Astrophysics, John Wiley & Sons
- Ridgway, S.E. and Stockton A. 1997, AJ, 114, 511
- Rogers, A. E. E., et al. 1983, Science, 219, 51
- Schwab, F. R. and Cotton, W. D. 1983, AJ, 88, 688
- Shepherd, M. C., Pearson, T. J. & Taylor, G. B. 1994, BAAS, 26, 987
- Sparks, W. B., Biretta, J. A. and Macchetto, F. 1994, ApJS, 90, 909
- Sparks, W. B., Golombek, D., Baum, S. A., Biretta, J. A., De Koff, S., Macchetto, F., McCarthy, P., Miley, G.K. 1995, ApJ, 450, 55

This 2-column preprint was prepared with the AAS IATEX macros v4.0.

Fig. 1.— Maps of 3C264 at 5.0 GHz with different angular resolutions. For each map we list the instrument, the Gaussian beam used for convolution, the lower contour (at 3σ of the rms of the image) and the peak of brightness. In all cases contours increase in powers of 1.5. (a) EVN; 6 mas × 3.6 mas in P.A.70°; 0.6 mJy/beam; 0.126 Jy/beam. (b) EVN + MERLIN; 9.9 mas × 6.3 mas in P.A.70°; 0.3 mJy/beam; 0.137 Jy/beam. (c) EVN + MERLIN; 18.5 mas × 15.2 mas in P.A.72°; 0.3 mJy/beam; 0.155 Jy/beam. (d) EVN + MERLIN; 23.2 mas × 20.5 mas in P.A.68°; 0.3 mJy/beam; 0.160 Jy/beam. (e) EVN + MERLIN; 35.2 mas × 31.5 mas in P.A.50°; 0.3 mJy/beam; 0.165 Jy/beam. (f) EVN + MERLIN; 62 mas × 52 mas in P.A.47°; 0.35 mJy/beam; 0.170 Jy/beam.

Fig. 2.— (a) Flux density along the jet ridge line at radio (solid line) and optical (dashed line) wavelengths. Both brightness scales have been adjusted for display purposes. (b) Radio to optical spectral index. The dotted line represents the average value of the spectral index along the jet.

Fig. 3.— Flux density of the jet of 3C264 vs frequency. Straight lines represent independent linear fits for the radio and optical data. Asterisks correspond to Crane et al. (1993) data.

Fig. 4.— Evolution of physical parameters along the jet of 3C264. (a) Deconvolved jet FWHM vs distance from the core. The dotted lines represents the aperture of the jet used for the adiabatic model (see Section 4.1). (b) Minimum pressure at different positions along the jet, obtained from minimum energy conditions. (c-d) Magnetic field vs jet FWHM and distance from the core, respectively. The lines represent linear fits and the numbers the respective slopes.

Fig. 5.— Fits of CI, JP, and KP synchrotron spectral aging models to the overall spectrum of the jet of 3C264.

 $\label{table 1} \mbox{Table 1}$ Jet to Counter-Jet Constraints.

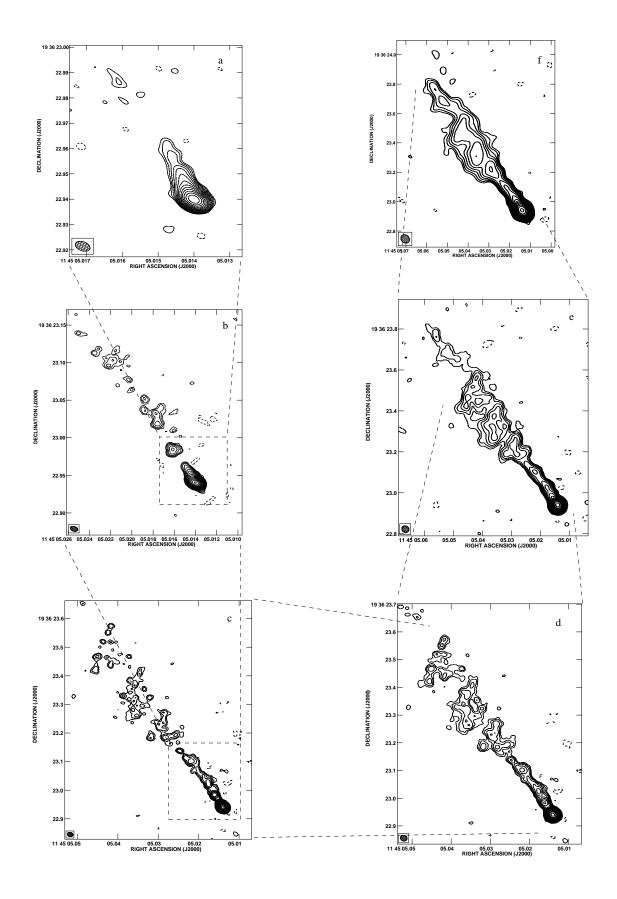
Distance (pc)	Brightness (mJy/beam)	R	$\beta \cos \theta$	beam (mas)
4	6.25	>9.9	>0.400	4.3×4.3
6	1.90	> 3.0	> 0.200	$4.3 {\times} 4.3$
8	1.86	> 3.0	> 0.200	4.3×4.3
10	1.25	> 2.0	> 0.128	4.3×4.3
20	5.55	> 18.5	> 0.493	23×20
30	1.47	> 4.9	> 0.286	23×20
40	2.75	> 9.2	> 0.389	23×20
50	1.58	> 5.3	> 0.299	23×20
60	1.19	> 4.0	> 0.251	23×20
70	0.91	> 3.0	> 0.200	23×20
80	1.80	> 6.0	> 0.320	23×20
120	5.98	> 16.6	> 0.477	108×89
144	8.06	> 22.4	> 0.519	108×89
160	8.76	> 24.3	> 0.530	108×89
200	5.69	> 15.8	> 0.470	108×89
240	5.85	> 16.3	> 0.475	108×89
320	2.78	> 7.7	> 0.361	108×89

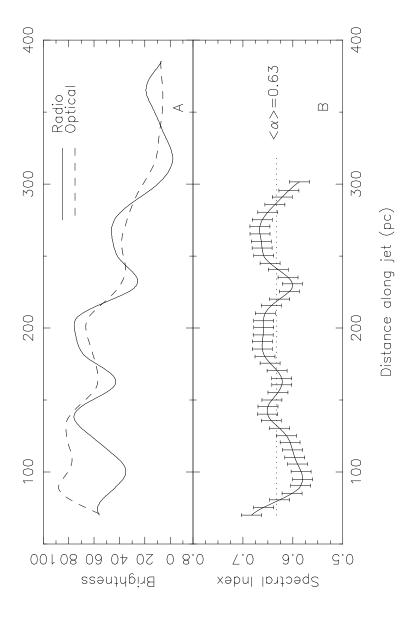
Table 2 3C264 Jet Flux Density.

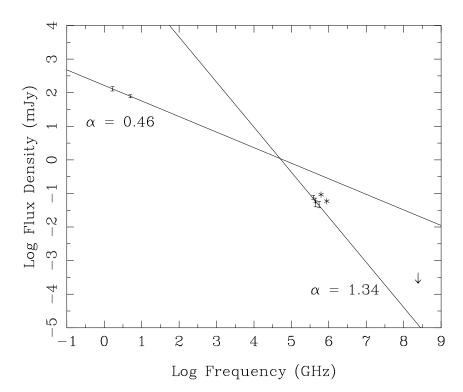
Frequency (GHz)	Flux Density (mJy)	References	
1.66	130.0	MERLIN data, to be published	
5.0	78.0	These data	
3.83e5	0.076	HST public archive	
4.35e5	0.062	BOG97	
4.46e5	0.049	HST public archive	
5.48e5	0.046	HST public archive	
6.18e5	0.093	Crane et al. 1993	
8.82e5	0.059	Crane et al. 1993	
242e6	< 0.0005	Prieto et al. 1996	

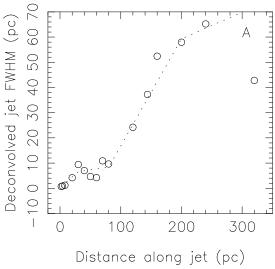
 $\label{eq:Table 3}$ Physical Parameters along the Jet of 3C264.

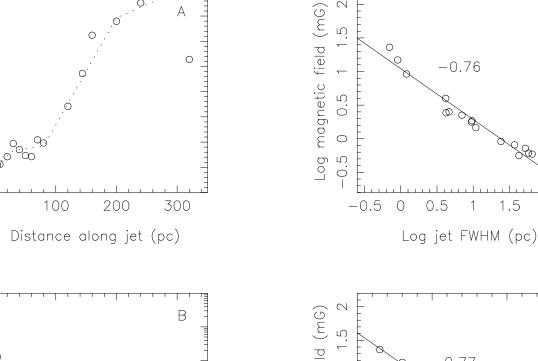
Distance (pc)	FWHM (pc)	Brightness $(Jy/asec^2)$	$\mathop{\rm B}_{me}_{(\eta^{-2/7} \text{ mG})}$	$\begin{array}{c} u_{me} \\ (\eta^{-4/7} \text{ erg/cm}^3) \end{array}$	$(\eta^{-4/7} \frac{P_{eq}}{\mathrm{dyn}/cm^2})$	$(\eta^{6/7} \mathrm{yr})$
0	0.29	52430	65.45	3.98×10^{-4}	2.46×10^{-4}	0.14
2	0.70	3242	22.97	4.90×10^{-5}	3.04×10^{-5}	0.74
4	0.91	917	14.86	2.05×10^{-5}	1.27×10^{-5}	1.42
8	1.20	224	9.18	7.81×10^{-6}	4.84×10^{-6}	2.92
20	4.18	42.2	4.00	1.48×10^{-6}	9.15×10^{-7}	10.2
30	9.43	5.50	1.77	2.90×10^{-7}	1.80×10^{-7}	35
40	7.00	9.34	2.24	4.64×10^{-7}	2.88×10^{-7}	24
50	4.64	9.20	2.51	5.82×10^{-7}	3.61×10^{-7}	20
60	4.21	7.48	2.43	5.47×10^{-7}	3.39×10^{-7}	21
70	10.89	3.23	1.46	1.96×10^{-7}	1.22×10^{-7}	46
80	9.64	6.67	1.85	3.19×10^{-7}	1.98×10^{-7}	32
120	24.20	1.38	0.91	7.67×10^{-8}	4.75×10^{-8}	94
144	37.24	1.40	0.81	6.04×10^{-8}	3.75×10^{-8}	112
160	52.42	1.29	0.72	4.75×10^{-8}	2.95×10^{-8}	134
200	57.96	0.81	0.61	3.43×10^{-8}	2.13×10^{-8}	171
240	65.22	0.80	0.59	3.19×10^{-8}	1.98×10^{-8}	181
320	42.8	0.45	0.56	2.91×10^{-8}	1.81×10^{-8}	193

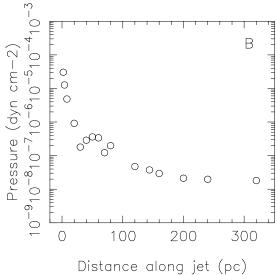


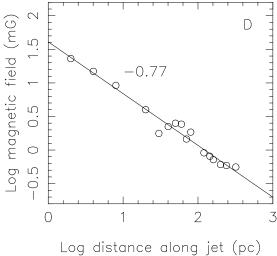












2.5

